HHS Public Access

Author manuscript

Nat Biomed Eng. Author manuscript; available in PMC 2023 March 27.

Published in final edited form as:

Nat Biomed Eng. 2023 March ; 7(3): 270–280. doi:10.1038/s41551-023-01003-7.

Near-infrared fluorescence lifetime imaging of amyloid-β aggregates and tau fibrils through the intact skull of mice

Steven S. Hou[1], **Joyce Yang**[1], **Jeong Heon Lee**[2], **Yeseo Kwon**[1], **Maria Calvo-Rodriguez**[1], **Kai Bao**[2], **Sung Ahn**[2], **Satoshi Kashiwagi**[2], **Anand T. N. Kumar**[3], **Brian J. Bacskai**[1,✉], **Hak Soo Choi**[2,✉]

[1]Department of Neurology, Massachusetts General Hospital, Harvard Medical School, Boston, MA, USA

[2]Gordon Center for Medical Imaging, Massachusetts General Hospital, Harvard Medical School, Boston, MA, USA

[3]Athinoula A. Martinos Center for Biomedical Imaging, Massachusetts General Hospital, Harvard Medical School, Boston, MA, USA

Abstract

Non-invasive methods for the in vivo detection of hallmarks of Alzheimer's disease can facilitate the study of the progression of the disease in mouse models and may enable its earlier diagnosis in humans. Here we show that the zwitterionic heptamethine fluorophore ZW800–1C, which has peak excitation and emission wavelengths in the near-infrared optical window, binds in vivo and at high contrast to amyloid-β deposits and to neurofibrillary tangles, and allows for the microscopic imaging of amyloid-β and tau aggregates through the intact skull of mice. In transgenic mouse models of Alzheimer's disease, we compare the performance of ZW800–1C with that of the two spectrally similar heptamethine fluorophores ZW800–1A and indocyanine green, and show that ZW800–1C undergoes a longer fluorescence-lifetime shift when bound to amyloid-β and

✉**Correspondence and requests for materials** should be addressed to Brian J. Bacskai or Hak Soo Choi. bbacskai@mgh.harvard.edu; hchoi12@mgh.harvard.edu.

Author contributions

S.S.H., J.H.L., B.J.B. and H.S.C. conceived the study and designed the experiments. S.S.H., J.Y., S.A. and Y.K. performed the ex vivo imaging experiments and analysed the results. S.S.H., J.Y., J.H.L., Y.K., M.C.-R. and S.K. performed the in vivo validation experiments and analysed the results. K.B. synthesized the compounds used in the study (ZW800-1A and ZW800-1C). S.S.H. and A.T.N.K. performed the fluorescence lifetime measurements and interpreted the results. S.S.H., B.J.B. and H.S.C. wrote the manuscript. B.J.B. and H.S.C. supervised the entire project. All authors approved the final version of the manuscript.

Competing interests

The authors declare no competing interests.

Reporting summary

Further information on research design is available in the Nature Portfolio Reporting Summary linked to this article.

Code availability

The custom ImageJ and Matlab codes are available on request from the corresponding authors.

Extended data is available for this paper at https://doi.org/10.1038/s41551-023-01003-7.

Supplementary information The online version contains supplementary material available at https://doi.org/10.1038/s41551-023-01003-7.

Peer review information *Nature Biomedical Engineering* thanks Jan Klohs and the other, anonymous, reviewer(s) for their contribution to the peer review of this work.

tau aggregates than when circulating in blood vessels. ZW800–1C may prove advantageous for tracking the proteinic aggregates in rodent models of amyloid-β and tau pathologies.

Alzheimer's disease (AD) is a fatal neurodegenerative disorder characterized by progressive cognitive impairment and neurodegeneration. The hallmark neuropathological features of the disease are the extracellular senile plaques formed from the aggregation of the amyloid-β peptide and the neurofibrillary tangles (NFTs) formed by hyperphosphorylation of the tau protein. Currently, the confirmed diagnosis of AD depends on post-mortem identification of amyloid plaques and NFTs in the brain[1]. To enable early diagnosis of AD and to better study disease progression in human patients and mouse models, there is an urgent need to develop improved methods for non-invasive imaging of both hallmarks in the living brain[2,3].

The most common imaging modalities for imaging AD pathology are magnetic resonance imaging (MRI)[4–7], position emission tomography (PET)[8–10], single-photon emission computed tomography (SPECT)[11–13] and optical imaging techniques[14–17]. Optical techniques for imaging AD offer several advantages, including the use of safe non-ionizing radiation, high sensitivity, wide availability, and the low cost and portability of the instrumentation[18–21]. In contrast to MRI and radiolabelling techniques, optical imaging is the only imaging modality with the theoretical spatial and temporal resolution to allow the in vivo visualization of individual amyloid plaques and NFTs. To perform in vivo imaging using optical techniques, there has been substantial work to develop red-shifted optical probes[22,23]. This is motivated by the well-known phenomenon that photon scattering decreases as wavelength increases with a fourth power dependence, which results in a greater penetration depth when imaging at longer wavelengths[24]. In addition, absorption due to chromophores, such as haemoglobin, and water is relatively low in the near-infrared (NIR) window (700–1,000 nm), allowing for increased tissue penetration[18,19,23]. Furthermore, fluorescence imaging at longer wavelengths has a lower background due to a decrease in tissue autofluorescence[23].

Several NIR fluorophores have been published for imaging of amyloid-β pathology[14,25–32]. However, most published probes have excitation and emission peak wavelengths in the 600–650 nm range, and to our knowledge, none of the published fluorescent probes for AD have both excitation and emission peak wavelengths within the 700–1,000 nm range where the tissue penetration is maximized. In addition, there have been comparatively fewer reports of optical probes for imaging NFTs than amyloid-β, especially at longer wavelengths[33–37]. Here we show that ZW800–1C[38,39], a NIR heptamethine fluorophore with peak excitation (753 nm) and emission (772 nm) wavelengths in the NIR window, can serve as a versatile probe for in vivo AD imaging. We fully characterize ZW800–1C and demonstrate its ability to cross the blood–brain barrier (BBB) in transgenic (Tg) mouse models of AD and bind to both amyloid-β and tau aggregates. As part of our characterization study, we compare the performance of ZW800–1C with two spectrally and structurally similar heptamethine fluorophores, indocyanine green (ICG)[40] and ZW800–1A[41]. ICG is a widely used NIR fluorophore that is US Food and Drug Administration (FDA)-approved for clinical use, while ZW800–1A is a hydrophilic derivative of ZW800–1C. We exploit the long excitation/emission wavelengths of ZW800–1C to image amyloid

plaques, cerebral amyloid angiopathy (CAA) and NFTs through the intact skull. The results show that non-invasive imaging of AD pathology in mice is feasible. We also show the potential of ZW800–1C as a lifetime-sensitive fluorophore for AD detection, which could have important applications for non-invasive tomographic imaging in the whole brain using fluorescence lifetime tomography[42,43].

Results

ZW800–1C labels amyloid-β and tau aggregates ex vivo in AD mouse and human tissue sections

To validate ZW800–1C as an AD imaging probe, we compare its performance to ZW800–1A, which possesses a fragile and flexible oxygen-based central linker in place of a carbon-carbon (C-C) bond (Fig. 1a). The relatively hydrophobic C-C linker of ZW800–1C results in higher hydrophilicity (log$D$; −2.80 at pH 7.4) and lower topological polar surface area (TPSA) (157.95 Å^2) values compared with ZW800–1A (Table 1). The excitation/emission spectra for the three NIR fluorophores in our study are shown in Fig. 1b. Before in vivo validation of ZW800–1C, we tested its ability to specifically label amyloid-β and tau aggregates ex vivo in brain tissue sections and compared its binding properties with ICG and ZW800–1A. For the mouse model of cerebral amyloidosis, we used the APPswe/PSEN1ΔE9 (APP/PS1) model, which develops amyloid-β pathology starting at 5–6 months and has dense pathology at 9 months[44]. As the model of tauopathy, we used the rTg4510 mouse model, which starts development of NFTs at 2 months of age[45]. We used the histochemical probe thioflavin S (ThioS) as a counterstain for labelling amyloid plaques, CAA and NFTs. ThioS is considered a gold standard for labelling AD pathology and emits blue-green fluorescence with a peak emission of ~480 nm when bound to pathology[46,47]. Co-labelling with ThioS and each NIR fluorophore was achieved by first incubating the tissue section in ThioS, washing in ethanol, incubating in the NIR fluorophore and finally washing in PBS.

Widefield epifluorescence microscopy was used to image the tissue sections in the green and NIR spectral channels. In APP/PS1 tissue (Fig. 2a), we found exact co-localization of the ThioS-positive aggregates with both ICG and ZW800–1C-positive aggregates, demonstrating that ICG and ZW800–1C have high specificity for amyloid-β aggregates. In contrast, ZW800–1A showed no apparent specificity for amyloid-β aggregates. Notably, in ZW800–1C-stained tissue sections, we also found a significant difference in labelling intensity between plaques and CAA, with CAA being 3.1-fold brighter than plaques, indicating that ZW800–1C preferentially labels CAA over plaques (Extended Data Fig. 1). We also verified that ZW800–1C successfully labels amyloid plaques (Supplementary Fig. 1a,b) and CAA (Supplementary Fig. 1c) in human AD tissue sections. To further characterize the specificity of ZW800–1C binding to amyloid-β, we performed in vitro binding assays with synthetic human amyloid-β aggregates. We found that ZW800–1C shows fluorescence enhancement of 3.9-fold when binding to Aβ40 aggregates and 1.8-fold when binding to Aβ42 aggregates (Supplementary Fig. 2a). In addition, we observed a spectral shift of the ZW800–1C emission peak from 772 nm to 791 nm when mixed with Aβ40 and to 781 nm when mixed with Aβ42. Similarly, we found that ZW800–1C undergoes a shift in fluorescence lifetime when mixed with amyloid-β aggregates

(Supplementary Fig. 2b). The lifetime of ZW800–1C was measured to be 0.55 ns in PBS, while adding Aβ40 and Aβ42 increased the lifetime to 1.03 ns and 0.92 ns, respectively. We determined the binding constant for ZW800–1C to be K_d = 43.7 ± 5.8 nM for Aβ40 aggregates (Supplementary Fig. 2c) and K_d = 78.9 ± 12.3 nM for Aβ42 aggregates (Supplementary Fig. 2d). In rTg4510 tissue sections (Fig. 2b), we found co-localization between the ThioS and ZW800–1C-positive cells in the staining of NFTs. In contrast, both ICG and ZW800–1A-stained tissue sections only showed a uniform background fluorescence with no apparent specificity for NFTs.

ZW800–1C binds to amyloid aggregates in vivo in APP/PS1 mice and can be detected by confocal microscopy

To simultaneously image visible and NIR fluorophores in vivo, we built a custom multimodal microscope (schematic shown in Supplementary Fig. 3). Our microscope enables confocal imaging of NIR fluorophores and multiphoton imaging of visible and NIR fluorophores. We next proceeded to evaluate the ability of ICG, ZW800–1A and ZW800–1C to cross the BBB and label amyloid plaques and CAA in the APP/PS1 mouse model (Fig. 3a). Mice were implanted with cranial windows at least 3 weeks before imaging. Methoxy-X04 (MX04) was also injected intraperitoneally 1 d before imaging to confirm the labelling of amyloid plaques and CAA in vivo[15]. Of each NIR fluorophore, 50 nmol were injected intravenously through the retro-orbital sinus, and mice were imaged 2 h post-injection using confocal microscopy with excitation at 770 nm. We validated the labelling of amyloid-β aggregates by sequential imaging with two-photon microscopy of MX04 at 770 nm. Representative images of CAA (Fig. 3b) and plaques (Fig. 3c) are shown with the same intensity scale among the three fluorophores. We also acquired a series of measurements to demonstrate the difference in labelling intensity of each NIR fluorophore when binding to the same amyloid plaque and CAA segment (Supplementary Fig. 4). To obtain a quantitative estimate for the difference in labelling intensity among the three fluorophores, 6–8 volumes containing plaques and 4–5 volumes containing CAA were acquired for each mouse, and the average plaque and CAA intensity was calculated for each fluorophore (Fig. 3d). In mice injected with ZW800–1C, we found bright labelling of both amyloid plaques and CAA, signifying that the fluorophore successfully crosses the BBB. We found that ZW800–1C labels CAA at 4.8-fold the intensity of plaques, consistent with our previous observation ex vivo. In mice injected with ZW800–1A, both amyloid plaques and CAA were labelled by the fluorophore, with the labelling intensity being significantly less than with ZW800–1C. In mice injected with ICG, we did not observe any labelling of amyloid plaques. However, we did find that ICG labels the CAA around a subset of vessel branches while not labelling the CAA around other branches (Extended Data Fig. 2 shows examples of CAA vessels with and without ICG labelling). We did not observe this phenomenon of selective labelling of either amyloid plaques or CAA with ZW800–1A and ZW800–1C. In non-transgenic littermates, we did not observe any substantial non-specific labelling after injection of the NIR fluorophores, although we did observe some low-intensity peri-arterial labelling for all three NIR fluorophores (Extended Data Fig. 3a). To further validate that ZW800–1C can label amyloid pathology in vivo, we also performed ex vivo imaging of brain tissue sections obtained after in vivo co-injection of MX04 and ZW800–1C, which revealed co-localization between both fluorophores for amyloid plaques and CAA (Extended Data Fig. 4a,b).

Next, we characterized the in vivo biodistribution of ICG, ZW800–1A and ZW800–1C in the thoracic cavity, abdominal cavity and resected organs (Extended Data Fig. 5). At 4 h post-intravenous injection, both ZW800–1A and ZW800–1C displayed rapid renal clearance with minimal background tissue uptake except for the kidneys (Ki), while ICG showed hepatobiliary clearance through the gallbladder (Ga) and bile duct (BD) to the duodenum (Du). We used confocal imaging in the brain (Fig. 3e) and intermittent blood sampling from the tail vein to measure the in vivo kinetics of each NIR fluorophore in the blood. The short blood half-life ($t_{1/2}\beta$), area under the curve (AUC) versus time, clearance (Cl) and volume of distribution (V_d) indicate that ICG is rapidly extracted in hepatocytes and excreted to the intestine (In) within 4 h post-intravenous injection. On the other hand, ZW800–1C shows extended blood circulation ($t_{1/2}\beta$ = 41.36 min) and relatively high V_d (12.02 ml) compared with ICG and ZW800–1A, indicating increased biodistribution in tissue including the brain, relative to binding to plasma (Extended Data Fig. 5). To understand the clearance dynamics of the NIR fluorophores after labelling of amyloid pathology, we acquired time-lapse confocal images starting at 2 h after injection and imaging until 12 h post-injection. The labelling intensity, normalized to 2 h post-injection, showed similar rates of decay for all three NIR fluorophores, with intensities falling below 20% of the maximum intensity by 12 h post-injection (Fig. 3f).

ZW800–1C binds to NFTs in vivo in rTg4510 mice and can be detected by confocal microscopy

We next tested the ability of ICG, ZW800–1A and ZW800–1C to label NFTs in vivo (Fig. 4a). The rTg4510 mouse model was used as a model of tauopathy. To validate NFT labelling in vivo, we injected HS-84, a luminescent conjugated oligothiophene (LCO) that emits green fluorescence. We have previously shown that HS-84 successfully labels NFTs in vivo in rTg4510 mice and co-localizes with anti-tau antibodies in brain tissue sections[48,49]. Mice with cranial windows were injected with HS-84 7 d before imaging. Of each NIR fluorophore, 50 nmol were injected intravenously and imaged 2 h after the injection. In mice injected with ZW800–1C, we found strong labelling of cellular-sized structures. We verified co-localization between the HS-84 and ZW800–1C-labelled structures, signifying that ZW800–1C binds to NFTs in vivo (Fig. 4d). In contrast, we did not find any cellular labelling in mice injected with ICG and ZW800–1A (Fig. 4b,c). In rTg4510 non-transgenic littermates, we did not observe any cellular labelling but found similar levels of peri-arterial labelling as we found in APP/PS1 non-transgenic mice by all three NIR fluorophores (Extended Data Fig. 3b). We characterized the clearance of ZW800–1C after binding to NFTs and found that the labelling intensity decreased rapidly within the first 12 h and became negligible by 24 h after injection (Fig. 4e). In addition to in vivo imaging, we also performed ex vivo imaging of brain tissue sections after in vivo co-injection of HS-84 and ZW800–1C. The resulting images confirmed co-localization between NFTs labelled by HS-84 and ZW800–1C (Extended Data Fig. 4c).

Fluorescence lifetime can distinguish ZW800–1C within blood vessels and bound to AD pathology

We next used in vivo confocal microscopy and fluorescence lifetime imaging microscopy (FLIM) based on the time-correlated single-photon counting technique to determine whether

ZW800–1C undergoes lifetime changes after binding to AD pathology. ZW800–1C was intravenously injected into C57BL/6J, APP/PS1 and rTg4510 mice, and representative fluorescence lifetime images are shown in Fig. 5a–e. In C57BL/6J mice, the average lifetime of ZW800–1C in blood vessels was measured to be 0.84 ns (Fig. 5a). After injection into APP/PS1 mice, we observed that ZW800–1C lifetime increased relative to the blood vessel after binding to CAA (Fig. 5b). By 2 h after injection, both CAA (Fig. 5c) and plaques (Fig. 5d) showed substantially longer lifetimes compared with blood vessels, with an average lifetime of 1.24 ns for plaques and 1.27 ns for CAA. In rTg4510 mice, we also observed an increase in the lifetime of ZW800–1C bound to NFTs, with the average lifetime measured to be 1.14 ns (Fig. 5e). Figure 5f shows the average temporal decay of fluorescence from blood vessel, amyloid-β and tau aggregates. When the distribution of lifetimes of ZW800–1C inside blood vessels is compared with the distribution of lifetimes of ZW800–1C bound to amyloid-β and tau aggregates, there was a clear separation among all three groups (Fig. 5g). This result indicates that the fluorescence lifetime of ZW800–1C could be used to distinguish the different pathological hallmarks from other sources of background fluorescence, such as in the blood vessel and autofluorescence. In addition to ZW800–1C, we also explored fluorescence lifetime imaging with ICG and ZW800–1A (Extended Data Fig. 6). ICG showed a small decrease in lifetime when bound to CAA (0.67 ns) as compared with in blood vessels (0.77 ns). For ZW800–1A, we found that there was a notable separation in lifetime between CAA (0.98 ns) and amyloid plaques (0.84 ns), which both differed from the lifetime found within blood vessels (0.64 ns).

Long-wavelength two-photon microscopy of ZW800–1C enables non-invasive fluorescence lifetime imaging of AD pathology

Using single-photon excitation with confocal microscopy, we showed that ZW800–1C bonded to amyloid-β and tau aggregates in vivo and resulted in the brightest fluorescence intensity among the three tested NIR fluorophores. We next attempted to exploit the long-wavelength spectral properties of ZW800–1C to pursue deep tissue imaging using two-photon microscopy. We first measured the two-photon absorption spectrum of ZW800–1C and found that within the tunable range of our laser, the peak absorption occurred at the maximum laser wavelength of 1,300 nm (Fig. 6a). Using two-photon microscopy, we sought to confirm the ability of ZW800–1C to penetrate the BBB by directly measuring the temporal dynamics of ZW800–1C after entering the brain. In a cohort of 3-month-old C57BL/6J mice, ZW800–1C was injected intravenously, and two-photon imaging data were acquired from 10 min to 8 h post-injection. In all mice, we observed that fluorescence accumulated around cells within the brain parenchyma upon intravenous administration, signifying that ZW800–1C can cross the BBB in healthy mice (Fig. 6b). Overall, ZW800–1C cleared slowly out of the brain, with its fluorescence intensity declining to 69% of its peak value at 8 h post-injection (Fig. 6c). Next, we used two-photon microscopy with ZW800–1C to image AD pathology in APP/PS1 and rTg4510 mice. Mice with cranial windows were intravenously injected with both ZW800–1C and 70 kDa Alexa Fluor 680 to create a fluorescent angiogram. We found that two-photon excitation of ZW800–1C at 1,300 nm was sufficiently bright for imaging amyloid plaques, CAA and NFTs with high contrast (Extended Data Fig. 7a–c).

To further characterize the in vivo performance of ZW800–1C, we compared the contrast to noise ratio (CNR) from in vivo measurements with that from ex vivo tissue staining measurements. We found that the average CNR obtained in vivo was higher than that obtained ex vivo for both amyloid plaques (10.8 for ex vivo, 81.2 for in vivo) and NFTs (2.5 for ex vivo, 6.9 for in vivo) (Fig. 6d,e). To demonstrate the feasibility of imaging ZW800–1C at depth, we acquired two-photon volumes in both young (7–8 months old) and old (22–24 months old) APP/PS1 mice (Extended Data Fig. 7d). We found that in the young mice group, amyloid plaques could be imaged with high contrast throughout a volume reaching at least 700 μm below the surface of the brain. However, in the old mice group, the maximum penetration depth was reduced such that even images acquired at 600 μm below the surface were noticeably blurred. This difference in achievable penetration depth between the two age groups is probably due to the thicker dura in the old mice group. We quantified the percentage volume of the brain occupied by plaques in both groups and as expected, we found substantially higher plaque volumes in the old cohort (0.52%) compared with the young cohort (0.06%) (Extended Data Fig. 7e).

Finally, we tested the feasibility of non-invasive imaging through the intact skull (Fig. 6f). In a cohort of 8–9-month-old APP/PS1 mice, the scalp was removed but the skull was left intact. The injection dosage of ZW800–1C was increased to 100 nmol to compensate for the attenuation of the excitation and emission light while travelling through the skull. At 2 h post-injection, we performed two-photon fluorescence lifetime imaging and found that both CAA and amyloid plaques could be successfully imaged through the intact skull (Fig. 6g,h and Supplementary Video 1). Similarly, we performed fluorescence lifetime imaging through the intact skull in a cohort of 6–8-month-old rTg4510 mice and found that NFTs could be detected with sufficient contrast to distinguish individual NFTs (Fig. 6i). Interestingly, we observed a decrease in average fluorescence lifetime when measuring through the intact skull as compared with measuring through a cranial window for both amyloid plaques (1.24 ns for cranial window, 1.05 ns for intact skull) and NFTs (1.14 ns for cranial window, 0.85 ns for intact skull) (Fig. 6j). This decrease in lifetime could be due to a larger contribution of a short lifetime background component when imaging through the intact skull as compared with imaging through a cranial window. We did not observe this lifetime shift for non-invasive imaging of CAA (1.27 ns for cranial window, 1.28 ns for intact skull), which we attribute to the superficial location of CAA in the brain. Our data suggest that two-photon imaging of ZW800–1C could be used to non-invasively monitor amyloid pathology with microscopic resolution through the intact skull.

Discussion

The development of NIR fluorescent probes for AD imaging is an active area of investigation that has produced several promising AD imaging agents in the past decade[14,25–34,37]. However, there have been few reports of NIR probes for AD with both excitation and emission wavelengths in the 700–1,000 nm range or that have affinity for both amyloid-β and tau. Among the reported probes suitable for in vivo imaging, the one with the longest excitation and emission wavelengths to our knowledge is CRANAD-58, which has peak excitation and emission wavelengths of 630 nm and 750 nm, respectively[29]. In this study, we fully characterized ZW800–1C as an imaging agent for AD that possesses

long peak excitation and emission wavelengths (753 nm and 772 nm) and can be used for imaging both amyloid-β and tau aggregates. We performed a full in vivo characterization study of ZW800–1C in AD transgenic mouse models and compared its binding properties and in vivo performance with two other heptamethine fluorophores, ICG and ZW800–1A.

When comparing the in vivo performance of the three heptamethine fluorophores, we found that ZW800–1C was the only fluorophore that was able to label all the main AD pathological hallmarks (amyloid plaques, CAA and NFTs) with high contrast. In addition to ZW800–1C's ability to bind to AD pathology, our biodistribution comparison study shows that ZW800–1C has rapid renal clearance and minimal non-specific tissue binding, which could contribute to the high contrast that we observe in vivo. Previous studies have attributed this non-specific tissue binding property of ZW800–1C to its zwitterionic charges[38,41]. One notable aspect of using ZW800–1C for imaging amyloid-β aggregates was the significantly higher brightness of CAA over amyloid plaques. Since this difference in labelling intensity occurs both when staining ex vivo brain sections and in vivo, it is probably not solely due to the proximity of CAA to blood vessels. This finding is also consistent with our in vitro binding assay result that ZW800–1C has a higher affinity for Aβ40 than Aβ42 aggregates since the main Aβ species in CAA and plaques are Aβ40 and Aβ42, respectively. Further work will be needed to elucidate how the probe interacts differently with CAA compared to amyloid plaques. Potential insights derived from this work could be invaluable for developing more CAA-specific probes and studying the pathological consequences of CAA. We found that ICG could label the CAA on a subset of blood vessels but could not label amyloid plaques and NFTs. Since ICG could label amyloid plaques and CAA after staining tissue sections ex vivo, we attribute ICG's inability to label all CAA segments and any amyloid plaques to its poor BBB penetrance. Therefore, a potential application for ICG could be to use its in vivo labelling pattern to determine which vessels with CAA may have BBB impairment. We found that ZW800–1A could label amyloid plaques and CAA at lower intensity compared with ZW800–1C, but could not label NFTs. This result can be explained by the high flexibility (TPSA = 167.18 Å^2) and hydrophilicity (log$D$ (pH 7.4) = −3.35) of ZW800–1A, which together could make it difficult to stay bound to the surface of amyloid-β and tau aggregates.

In this study, we do not investigate the mechanism by which the three heptamethine fluorophores can cross the BBB. Owing to the larger molecular sizes of the fluorophores, the amount of the fluorophore that crosses the BBB should be limited[50]. However, we observe the clear ability of each of the fluorophores to cross into the brain and target AD pathology. Even though one potential factor to explain our observations could be the previously reported increase in BBB permeability in AD mouse models[51], this cannot be the sole factor since we found that ZW800–1C also crosses the BBB in C57BL/6J mice. Alternatively, another possible explanation could be a carrier-mediated transport mechanism that allows the heptamethine fluorophores to cross into brain[52,53]. Further experiments will need to be conducted to understand the exact mechanism for our observed BBB crossing.

In addition to in vivo imaging with confocal microscopy using single-photon excitation, we also showed the feasibility of in vivo imaging using two-photon excitation of ZW800–1C at 1,300 nm. Two-photon microscopy provides better optical sectioning capability

than confocal microscopy and importantly, the longer excitation wavelength of 1,300 nm increases the laser penetration depth in tissue. These advantages have allowed us to image both amyloid and tau pathology through the intact mouse skull with microscopic resolution. Through-the-skull imaging with ZW800–1C opens the potential for non-invasive monitoring of AD pathology and assessment of therapeutic strategies at the cellular level when conducting preclinical mouse studies of AD.

Using FLIM, we showed that the lifetime of ZW800–1C substantially increased after binding to amyloid-β and tau aggregates compared with its lifetime when circulating in the blood. This change will allow increased sensitivity in differentiating AD pathology from other sources of fluorescence, such as intrinsic autofluorescence, especially in instances where the injection dosage is low. In general, lifetime contrast is especially relevant when considering the potential of translating NIR fluorescence techniques to human brain imaging. Since the human scalp is too thick to allow microscopic imaging with ballistic photons, NIR imaging would need to be performed using diffuse optical imaging with scattered photons. In this case, the ability of a candidate NIR fluorophore for AD imaging to possess amyloid-β or tau aggregate-dependent changes in fluorescence spectrum or lifetime will be critical for distinguishing between AD pathology and non-specific background binding and for providing quantitative measurements of pathological burden.

Methods

Animals

For imaging of amyloid-β aggregates, we used APP/PS1 (The Jackson Laboratory, B6.Cg-Tg (APPswe, PSEN1-dE9)85Dbo/Mmjax) double transgenic mice expressing mutant human APPswe/human PS1-ΔE9[44] along with age-matched non-transgenic littermates. Mice of both sexes were used at 8–9 months of age for through-skull imaging measurements and 10–12 months of age for in vivo characterization of candidate NIR fluorophores. For comparing different age groups, the young and old cohorts consisted of mice at 7–8 months and 22–24 months of age, respectively. For imaging neurofibrillary tangles, we used rTg4510 (The Jackson Laboratory, Tg (Camk2a-tTA)1Mmay Fgf14Tg (tetO-MAPT*P301L)4510Kh) mice expressing the tetracycline-controlled transactivator protein (tTA)[45]. Mice of both sexes at 6–8 months of age were used. C57BL/6J (The Jackson Laboratory) male mice at 3 months of age were used for blood pharmacokinetic studies, brain clearance and FLIM measurements. CD-1 (Charles River Laboratories) male mice at 6–8 weeks were used for biodistribution studies. Animals were housed in an AAALAC-certified facility (Massachusetts General Hospital, D16–00361), and all animal studies were performed under the supervision of the Massachusetts General Hospital Institutional Animal Care and Use Committee in accordance with the approved institutional protocol (2018N000131).

Ex vivo staining and imaging

APP/PS1 and rTg4510 mice were euthanized under CO_2 and transcardially perfused with PBS followed by 4% paraformaldehyde (PFA). Brains were extracted post-perfusion and incubated in 4% PFA solution at 4 °C for 1 d before being sliced into 40 μm sections on a microtome. The free-floating sections were then stored in cryoprotectant (30% sucrose

in 0.1 M phosphate buffer) at −20 °C until the day of staining. Ex vivo co-staining was carried out on mouse and human AD tissue sections by sequential staining of ThioS and each NIR fluorophore. Free-floating sections were first incubated for 8 min in 0.05% ThioS in 50% ethanol and then rinsed with 3 washes of 80% ethanol, followed by PBS for 5 min. Next, sections were incubated in 100 μM of the NIR fluorophore in PBS for 8 min, rinsed with 3 washes of PBS and immersed in PBS for 5 min. Tissue sections were mounted with Vectashield in preparation for widefield epifluorescence imaging. Slides were imaged on an Olympus BX51 microscope using a ×25 objective (1.05 NA, Olympus), with a green fluorescent protein filter cube for ThioS and NIR filter cube for each heptamethine fluorophore.

In vitro binding assays

For creating amyloid-β aggregates, 40 μl of 1.0% NH_4OH was added to 0.5 mg Aβ40 or Aβ42 peptide (AnaSpec). Next, PBS was added to create a 1 mg ml^{-1} solution. Of the resulting solution, 100 μl was further diluted 1:10 in PBS and gently shaken for 72 h at 37 °C to form aggregates. To test for interaction between ZW800–1C and amyloid-β aggregates, fluorescence spectra were measured using a Vis-NIR spectrometer (Ocean Optics). A Ti-Sapphire laser (Spectra Physics Mai Tai) tuned to 750 nm was used as the excitation source. Spectral measurements were taken with 1 μM ZW00–1C alone in PBS and mixed with either 5 μM Aβ40 or 5 μM Aβ42 aggregates. Fluorescence lifetime measurements were performed using the time-correlated single-photon counting technique with a NIR photomultiplier tube (PMT) (Hamamatsu H7422–50). Lifetime measurements were acquired for ZW800–1C at 25 nM in PBS and mixed with either 500 nM Aβ40 or 500 nM Aβ42 aggregates. For binding affinity measurements, fluorescence intensities were acquired for ZW800–1C alone at various concentrations and then after mixing with either 500 nM Aβ40 or 500 nM Aβ42 aggregates.

Surgical preparation and intravenous delivery

Cranial window surgery was performed as previously described[54] with minor modifications. Briefly, mice were anaesthetized with isoflurane (1–1.5%), and a craniotomy was performed over the right hemisphere by removal of a ~5 mm piece of the skull above the somatosensory cortex. The dura mater was left intact during the craniotomy procedure. A 5-mm-diameter cover glass was placed over the exposed brain and sealed with a mixture of dental acrylic and cyanoacrylate glue. After the cranial window surgery, mice were given buprenorphine (0.1 mg kg^{-1}) and Tylenol for 3 d after surgery, and were allowed to recover for at least 3 weeks before imaging experiments. For non-invasive imaging through the intact skull, a 5-mm-diameter cover glass was glued to the exposed skull surface using an ultra-violet curable glue (Loctite 4305) as previously described[55]. Mice were given buprenorphine (0.1 mg kg^{-1}) and imaged on the day of the procedure. To validate NFT labelling in rTg4510 mice, 150 nmol of the LCO (HS-84 in 150 μl PBS) was intravenously delivered via retro-orbital injection. HS-84 was injected 7 d before the imaging experiment. In APP/PS1 mice, 363 nmol of MX04 in 300 μl PBS was delivered via intraperitoneal injection 24 h before imaging. ZW800–1A and ZW800–1C were synthesized as previously described[38] and a 10 mM stock solution was created in 50% H_2O and 50% dimethyl sulfoxide (DMSO). NIR fluorophores were intravenously delivered via retro-orbital injection. In mice with cranial

windows, the dosage amount was 50 nmol of each NIR fluorophore in 200 μl PBS, while for imaging through the intact skull with ZW800–1C, the dosage amount was increased to 100 nmol.

In vivo confocal and multiphoton imaging

In vivo imaging was performed with a custom multimodal optical imaging system that combines confocal and multiphoton microscopy for imaging of NIR fluorophores. The main microscope body including the epifluorescence module consists of components from a modular microscopy platform (Thorlabs Cerna Series). A galvo-resonant scanner (Sutter Instrument) is used for fast scanning of the laser source. An Olympus ×25 dipping objective (NA = 1.05) is used for both confocal and multiphoton measurements. The excitation source for the system consists of either the combination of a Ti:sapphire laser (Spectra Physics Mai Tai) pumping an optical parametric oscillator (Spectra Physics Opal) or a widely tunable Ti-sapphire laser (Spectra Physics Insight X3). The Ti:sapphire is operated at 770 nm for single-photon excitation of the heptamethine fluorophores or for two-photon excitation of Methoxy-X04 and HS-84. The optical parametric oscillator is operated at 1,300 nm for two-photon excitation of ZW800–1C. For the confocal microscopy light path, the system uses a NIR-sensitive GaAsP PMT (Hamamatsu H7422–50) with an 845/55 nm emission filter (Chroma) to detect NIR fluorescence from all heptamethine fluorophores. A 100 μm pinhole (Thorlabs) is incorporated into the detection path to filter out scattered fluorescence. For the multiphoton microscopy light path, a NIR-sensitive GaAsP PMT (Hamamatsu H7422–50) is used with a 790/80 nm emission filter to detect NIR emission, and two GaAsP PMTs (Hamamatsu H10770B-40) are used with 460/50 nm and 525/50 nm emission filters (Chroma) to detect visible fluorescent emission. The output signals from the PMTs are either processed in analogue mode with a high-speed digitizer (National Instruments NI-5734) to produce intensity-based images with the ScanImage software[56] or in photon counting mode using a time-correlated single-photon counting module (Becker and Hickl SPC-150N) to produce FLIM images.

During in vivo imaging, mice were anaesthetized with 1.5% isoflurane in room air. Mice were placed on a microscope stage, with body temperature controlled with a heat pad (Kent). For in vivo characterization of the candidate NIR fluorophores, each fluorophore was first injected intravenously, and three-dimensional (3D) cortical volumes were acquired by confocal microscopy at a resolution of 512 × 512 pixels and from 0–200 μm below the surface of the brain. The laser power and PMT settings were kept constant for all measurements to allow quantitative comparison between animals. For two-photon measurements with ZW800–1C, 70 kDa Alexa Fluor 680 was retro-orbitally injected before imaging to provide a fluorescent angiogram.

In vivo characterization of biodistribution and clearance

To investigate the biodistribution and clearance of each NIR fluorophore, 250 μM working solutions were prepared in 5% bovine serum albumin (BSA). Then, 100 μl (25 nmol) of each NIR fluorophore was intravenously injected into 6-week-old CD-1 mice via the retro-orbital sinus under isoflurane anaesthesia. A custom-built real-time intraoperative NIR imaging system was used for white light and NIR fluorescence imaging[57]. After the imaging of

thoracic and abdominal cavities, mice were euthanized with CO_2 and the major organs including heart, lung, liver, pancreas, spleen, kidney, duodenum, intestine and muscle were excised and imaged for tissue-specific biodistribution.

Image analysis and statistical analyses

Three-dimensional imaging volumes were processed using the ImageJ/Fiji package (National Institutes of Health) and custom Matlab (Math-Works) scripts. Images presented in the figures are maximum intensity projections of 3D volumes. Data are presented as mean ± s.e.m. GraphPad Prism 9 was used for statistical analyses. Student's *t*-test was used to assess differences in labelling intensity between amyloid plaques and CAA, and one-way analysis of variance (ANOVA) was used to assess differences in labelling intensity among the NIR fluorophores. Two-way ANOVA was used to assess differences in organ biodistribution among the NIR fluorophores. A P value of less than 0.05 was considered significant. The data are indicated with $*P < 0.05$, $**P < 0.01$, $***P < 0.001$ and $****P < 0.0001$.

Extended Data

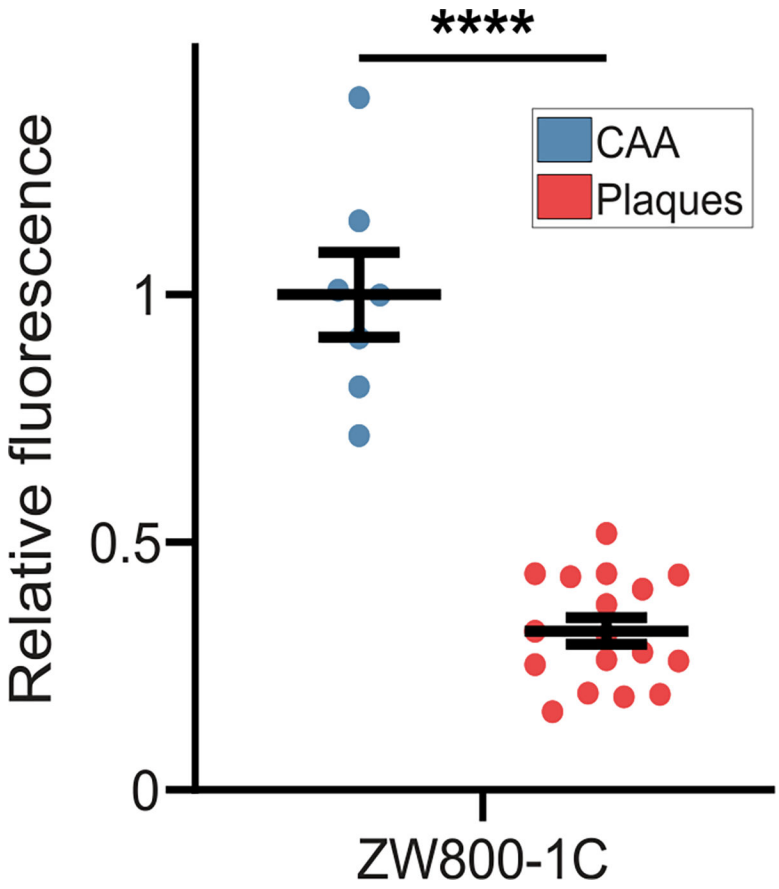

Extended Data Fig. 1 |. Ex vivo labeling intensity of amyloid plaques and CAA by ZW800–1C. Quantitative comparison of the average labeling intensity of CAA and plaques by ZW800–1C in APP/PS1 brain tissue sections. Sections were stained by incubation in 100 μM

ZW800–1C solution in PBS. Significance was calculated using unpaired two-tailed t-test: **** $P < 0.0001$. Data are shown as mean ± s.e.m.

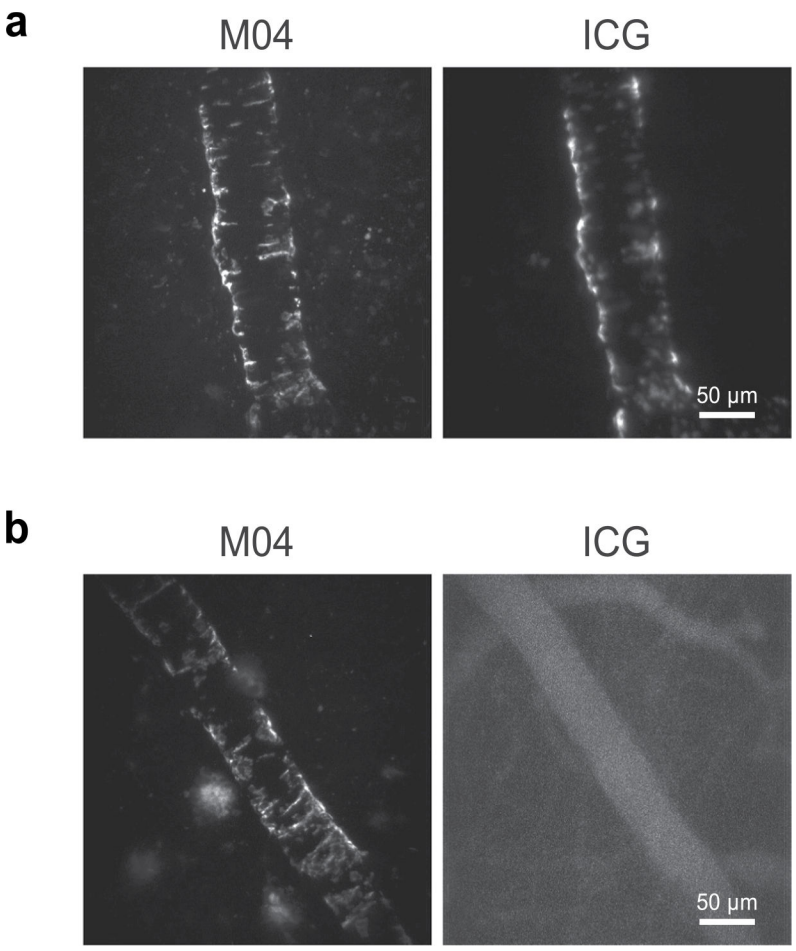

Extended Data Fig. 2 |. In vivo imaging reveals selective labeling of CAA with ICG in APP/PS1 mice.

Examples of arteries with CAA that are positively labeled with MX04 and (**a**) co-labeled with ICG and (**b**) not co-labeled with ICG. Images were acquired with confocal microscopy at 2 h post-injection.

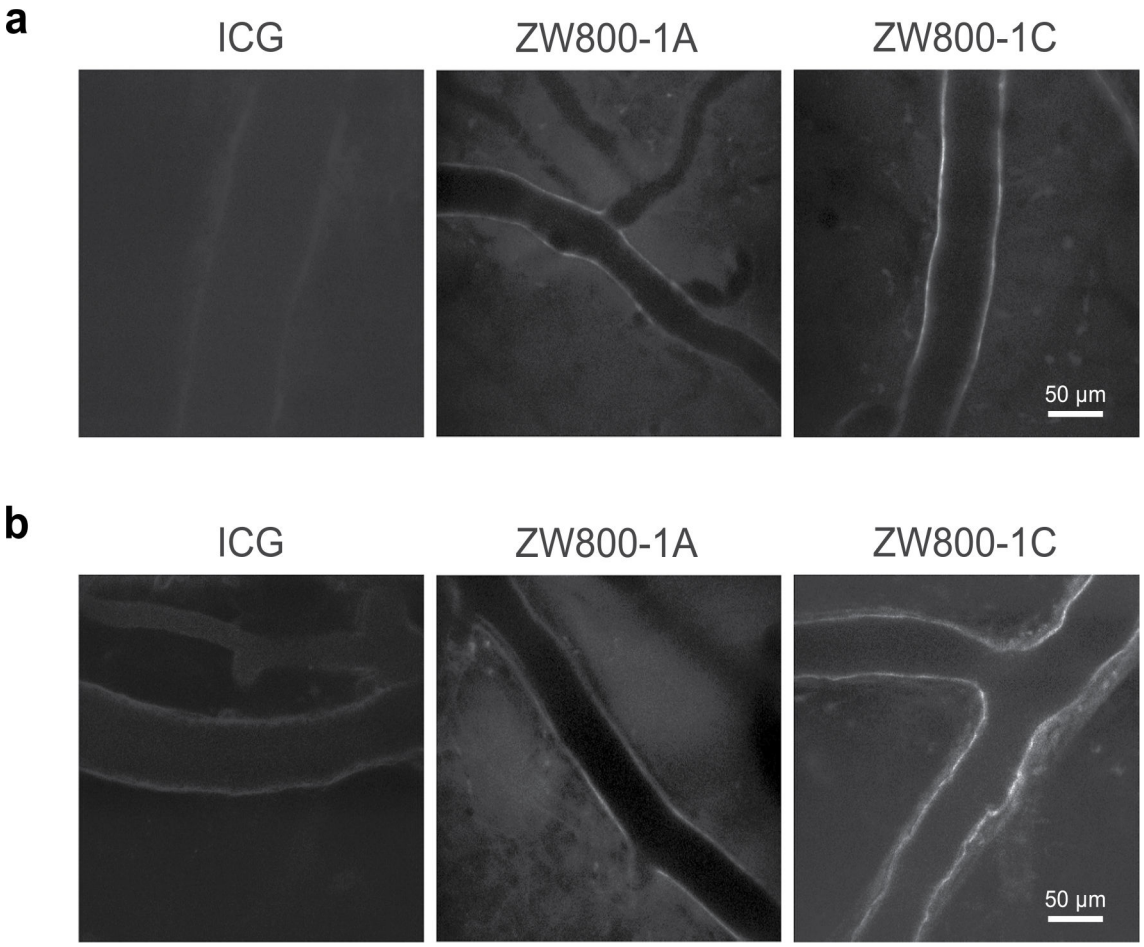

Extended Data Fig. 3 |. In vivo imaging of ICG, ZW800–1A, and ZW800–1C in APP/PS1 and rTg4510 non-transgenic littermates.

Each NIR fluorophore was injected intravenously (50 nmol) and imaged 2 h post-injection with confocal microscopy. Representative images for both (**a**) APP/PS1 non-Tg littermates (n = 3) and (**b**) rTg4510 non-Tg littermates (n = 3) show low levels of periarterial labeling by all three fluorophores.

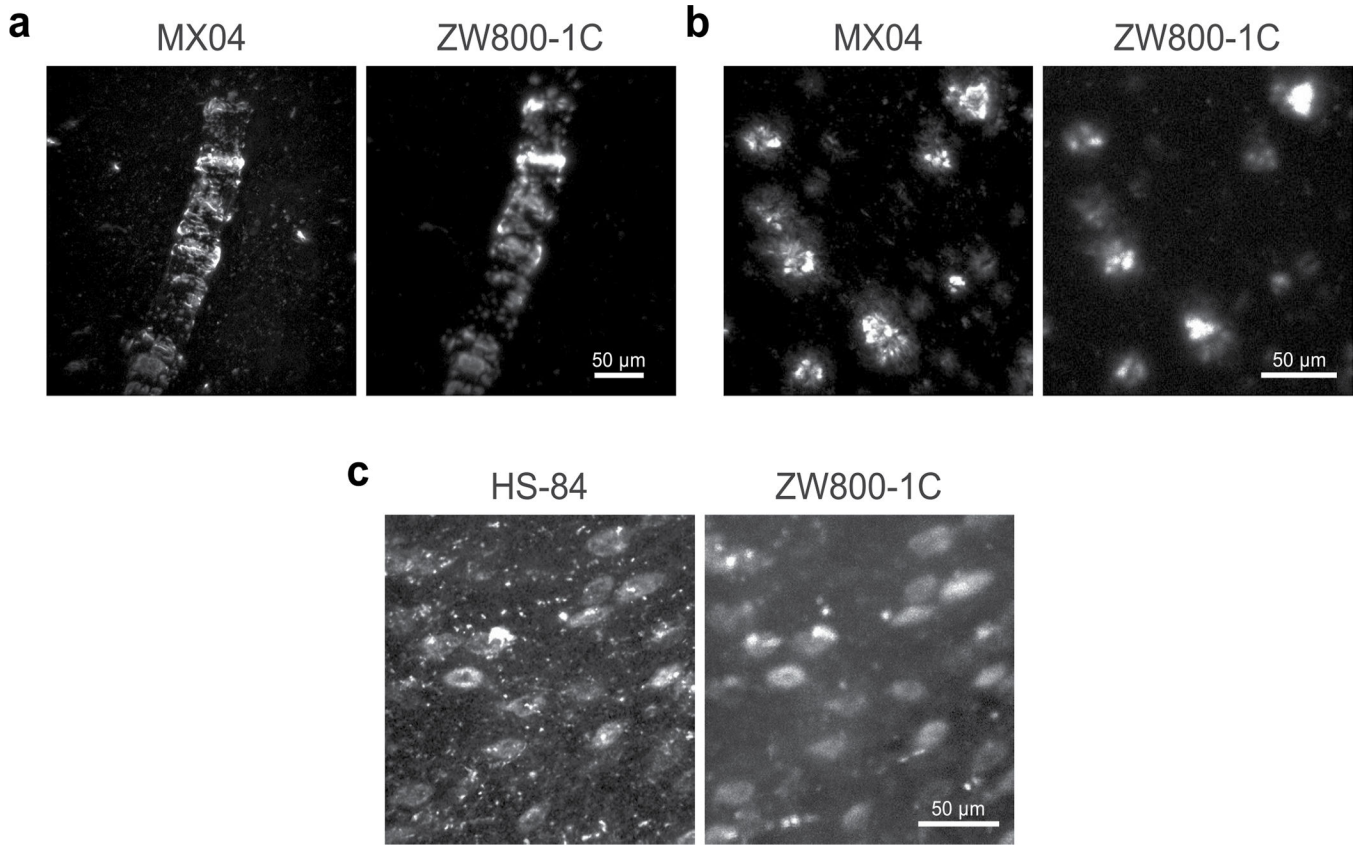

Extended Data Fig. 4 |. Post-mortem validation of ZW800–1C labeling in APP/PS1 and rTg4510 mice.

APP/PS1 mouse is intraperitoneally injected with MX04 and intravenously injected with ZW800–1C at 24 h and 2 h before sacrifice. Ex vivo imaging is performed on brain tissue sections, and representative images show co-stained (**a**) CAA and (**b**) amyloid plaques. (**c**) Tg4510 mouse is intravenously injected with HS-84 and ZW800–1C at 7 days and 2 h before sacrifice, respectively. Representative images show co-labeling of NFTs.

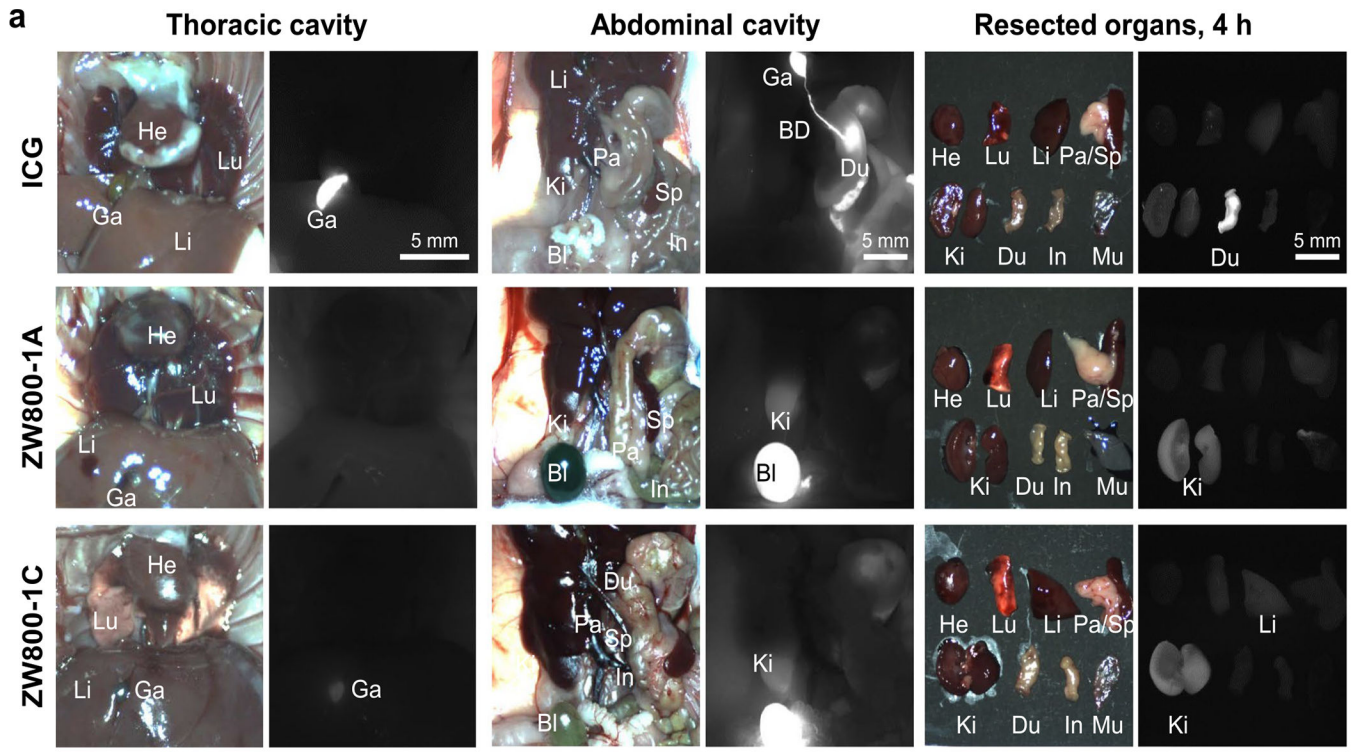

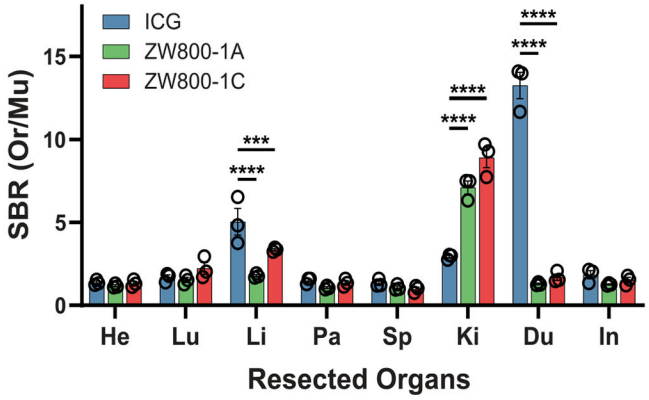

c

PK parameter	ICG	ZW800-1A	ZW800-1C
$t_{1/2}\alpha$ (min)	N/A	3.90	2.99
$t_{1/2}\beta$ (min)	5.74	32.38	41.36
AUC (%ID/g • min)	455	890	1,191
Cl (mL/min)	0.66	0.27	0.20
V_d (mL)	5.46	12.60	12.02
Urine (%ID)	< 5.0	> 80	< 50

Extended Data Fig. 5 |. In vivo biodistribution study of ICG, ZW800–1A, and ZW800–1C in CD-1 mice.

25 nmol of ZW800–1C was injected in 25 g CD-1 mice 4 h prior to imaging. (**a**) Representative color and NIR images of ZW800–1C showing major organs in the thoracic cavity (left), abdominal cavity (middle), and after resection (right). (**b**) Signal-to-background ratio (SBR) of resected major organs (Or) against muscle (Mu). Abbreviations used are He, heart; Lu, lung; Li, liver; Pa, pancreas; Sp, spleen; Ki, kidney; Du, duodenum; Ga, gallbladder; BD, bile duct; Bl, bladder; In, intestine. ***$P = 0.0006$ and ****$P < 0.0001$ by two-way ANOVA with Dunnett's multiple comparison test. (**c**) Comparison of the pharmacokinetic parameters of the candidate NIR fluorophores. Abbreviations used are

$t_{1/2}\alpha$, distribution blood half-life; $t_{1/2}\beta$, elimination blood half-life; V_d, the volume of distribution; AUC, area under the curve; Cl, clearance. Data are shown as mean ± s.e.m.

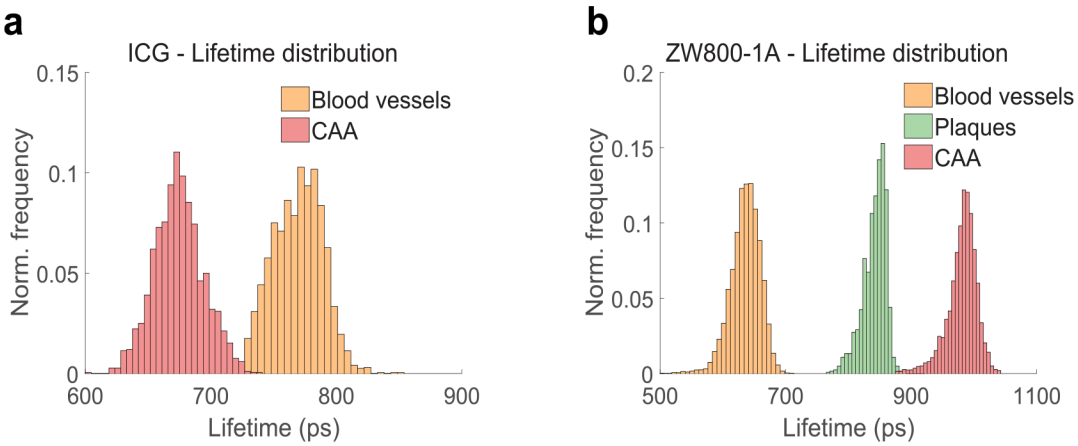

Extended Data Fig. 6 |. In vivo fluorescence lifetime imaging of ICG and ZW800–1A in C57BL/6J and APP/PS1 mice.

Histogram distribution of fluorescence lifetimes for (**a**) ICG and (**b**) ZW800–1A within blood vessels and after being bound to amyloid-β aggregates.

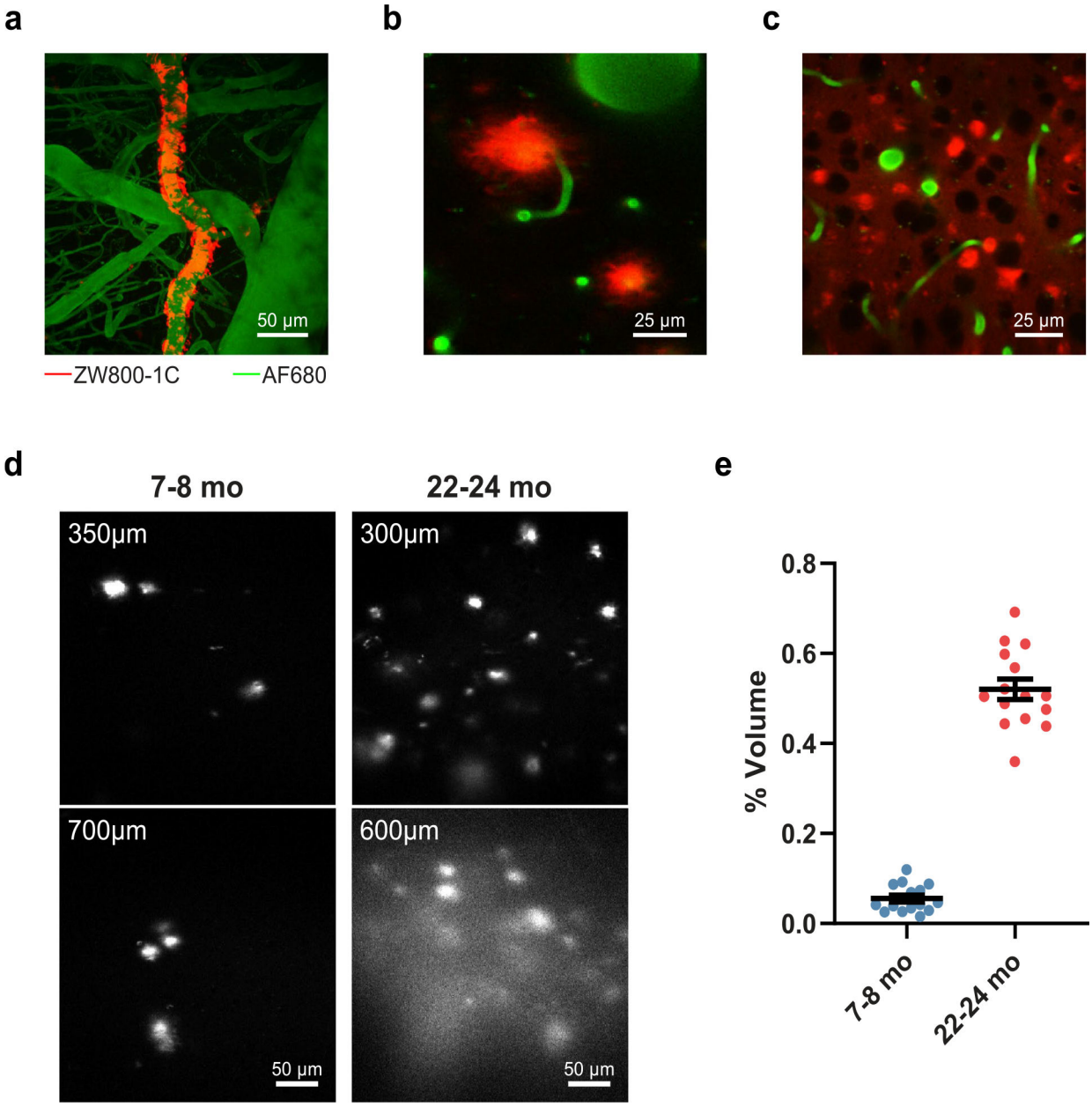

Extended Data Fig. 7 |. Two-photon imaging of ZW800–1C in APP/PS1 and rTg4510 mice. Two-photon imaging of ZW800–1C (red) with 1,300 nm excitation. Alexa Fluor 680–70 kDa Dextran (green) was systemically injected to create a fluorescent angiogram. Representative images show (**a**) CAA, (**b**) amyloid plaques and (**c**) NFTs from APP/PS1 (n = 3) and rTg4510 (n = 3) mice. (**d**) Images of amyloid plaques taken at different depths from 7–8 months old (mo) and 22–24 mo APP/PS1 mice. (**e**) Comparison of the percentage volume occupied by amyloid plaques for 7–8 mo and 22–24 mo APP/PS1 mice (n = 3 mice per age group). Data are shown as mean ± s.e.m.

Supplementary Material

Refer to Web version on PubMed Central for supplementary material.

Acknowledgements

We thank K. P. R. Nilsson for providing the HS-84 probe. This study was supported by grants from the National Institutes of Health (NIA R56AG060974 to B.J.B.; NIA K01AG072046 to S.S.H.; NCI R01CA211084 to A.T.N.K.; NIBIB R01EB022230 to H.S.C.) and the Creative Materials Discovery Program through the National Research Foundation of Korea (2019M3D1A1078938 to H.S.C.). The content expressed is solely the responsibility of the authors and does not necessarily represent the official views of the NIH.

Data availability

The main data supporting the results in this study are available within the paper and its Supplementary Information. The raw and analysed datasets generated during the study are available for research purposes from the corresponding authors on reasonable request. Source data are provided with this paper.

References

1. Montine TJ et al. National Institute on Aging–Alzheimer's Association guidelines for the neuropathologic assessment of Alzheimer's disease: a practical approach. Acta Neuropathol. 123, 1–11 (2012). [PubMed: 22101365]
2. Mathis C, Wang Y & Klunk W Imaging beta-amyloid plaques and neurofibrillary tangles in the aging human brain. Curr. Pharm. Des. 10, 1469–1492 (2005).
3. Villemagne VL, Doré V, Burnham SC, Masters CL & Rowe CC Imaging tau and amyloid-β proteinopathies in Alzheimer disease and other conditions. Nat. Rev. Neurol. 14, 225–236 (2018). [PubMed: 29449700]
4. Poduslo JF et al. Molecular targeting of Alzheimer's amyloid plaques for contrast-enhanced magnetic resonance imaging. Neurobiol. Dis. 11, 315–329 (2002). [PubMed: 12505424]
5. Flaherty DP et al. Polyfluorinated bis-styrylbenzene β-amyloid plaque binding ligands. J. Med. Chem. 50, 4986–4992 (2007). [PubMed: 17845017]
6. Martins AF et al. PiB-conjugated, metal-based imaging probes: multimodal approaches for the visualization of β-amyloid plaques. ACS Med. Chem. Lett. 4, 436–440 (2013). [PubMed: 24900692]
7. Chamberlain R et al. Magnetic resonance imaging of amyloid plaques in transgenic mouse models of Alzheimer's disease. Curr. Med. Imaging Rev. 7, 3–7 (2011). [PubMed: 21499442]
8. Mathis CA, Mason NS, Lopresti BJ & Klunk WE Development of positron emission tomography β-amyloid plaque imaging agents. Semin. Nucl. Med. 42, 423–432 (2012). [PubMed: 23026364]
9. Zhu L, Ploessl K & Kung HF PET/SPECT imaging agents for neurodegenerative diseases. Chem. Soc. Rev. 43, 6683–6691 (2014). [PubMed: 24676152]
10. Krishnadas N, Villemagne VL, Doré V & Rowe CC Advances in brain amyloid imaging. Semin. Nucl. Med. 51, 241–252 (2021). [PubMed: 33482999]
11. Zhuang ZP et al. Structure-activity relationship of imidazo[1,2-a] pyridines as ligands for detecting β-amyloid plaques in the brain. J. Med. Chem. 46, 237–243 (2003). [PubMed: 12519062]
12. Qu W, Kung MP, Hou C, Benedum TE & Kung HF Novel styrylpyridines as probes for SPECT imaging of amyloid plaques. J. Med. Chem. 50, 2157–2165 (2007). [PubMed: 17411026]
13. Valotassiou V et al. SPECT and PET imaging in Alzheimer's disease. Ann. Nucl. Med. 32, 583–593 (2018). [PubMed: 30128693]
14. Tong H, Lou K & Wang W Near-infrared fluorescent probes for imaging of amyloid plaques in Alzheimer's disease. Acta Pharm. Sin. B 5, 25–33 (2015). [PubMed: 26579421]

15. Klunk WE et al. Imaging Aβ plaques in living transgenic mice with multiphoton microscopy and methoxy-X04, a systemically administered Congo red derivative. J. Neuropathol. Exp. Neurol. 61, 797–805 (2002). [PubMed: 12230326]
16. Heo CH et al. A quadrupolar two-photon fluorescent probe for in vivo imaging of amyloid-β plaques. Chem. Sci. 7, 4600–4606 (2016). [PubMed: 30155107]
17. Teoh CL et al. Chemical fluorescent probe for detection of Aβ oligomers. J. Am. Chem. Soc. 137, 13503–13509 (2015). [PubMed: 26218347]
18. Ntziachristos V, Bremer C & Weissleder R Fluorescence imaging with near-infrared light: new technological advances that enable in vivo molecular imaging. Eur. Radiol. 13, 195–208 (2003). [PubMed: 12541130]
19. Ntziachristos V Fluorescence molecular imaging. Annu. Rev. Biomed. Eng. 8, 1–33 (2006). [PubMed: 16834550]
20. Frangioni JV In vivo near-infrared fluorescence imaging. Curr. Opin. Chem. Biol. 7, 626–634 (2003). [PubMed: 14580568]
21. Licha K & Olbrich C Optical imaging in drug discovery and diagnostic applications. Adv. Drug Deliv. Rev. 57, 1087–1108 (2005). [PubMed: 15908041]
22. Shcherbakova DM, Stepanenko OV, Turoverov KK & Verkhusha VV Near-infrared fluorescent proteins: multiplexing and optogenetics across scales. Trends Biotechnol. 36, 1230–1243 (2018). [PubMed: 30041828]
23. Hong G, Antaris AL & Dai H Near-infrared fluorophores for biomedical imaging. Nat. Biomed. Eng. 1, 0010 (2017).
24. Shi L, Sordillo LA, Rodríguez-Contreras A & Alfano R Transmission in near-infrared optical windows for deep brain imaging. J. Biophotonics 9, 38–43 (2016). [PubMed: 26556561]
25. Kim D et al. Two-photon absorbing dyes with minimal autofluorescence in tissue imaging: application to in vivo imaging of amyloid-β plaques with a negligible background signal. J. Am. Chem. Soc. 137, 6781–6789 (2015). [PubMed: 25951499]
26. Yang J et al. Oxalate-curcumin-based probe for micro- and macroimaging of reactive oxygen species in Alzheimer's disease. Proc. Natl Acad. Sci. USA 114, 12384–12389 (2017). [PubMed: 29109280]
27. Chen C et al. In vivo near-infrared two-photon imaging of amyloid plaques in deep brain of Alzheimer's disease mouse model. ACS Chem. Neurosci. 9, 3128–3136 (2018). [PubMed: 30067906]
28. Li Y et al. Fluoro-substituted cyanine for reliable in vivo labelling of amyloid-β oligomers and neuroprotection against amyloid-β induced toxicity. Chem. Sci. 8, 8279–8284 (2017). [PubMed: 29619173]
29. Zhang X et al. Design and synthesis of curcumin analogues for in vivo fluorescence imaging and inhibiting copper-induced cross-linking of amyloid beta species in Alzheimer's disease. J. Am. Chem. Soc. 135, 16397–16409 (2013). [PubMed: 24116384]
30. Cui M et al. Smart near-infrared fluorescence probes with donor-acceptor structure for in vivo detection of β-amyloid deposits. J. Am. Chem. Soc. 136, 3388–3394 (2014). [PubMed: 24555862]
31. Zhang X et al. Near-infrared fluorescence molecular imaging of amyloid beta species and monitoring therapy in animal models of Alzheimer's disease. Proc. Natl Acad. Sci. USA 112, 9734–9739 (2015). [PubMed: 26199414]
32. Fu H et al. Amyloid-β deposits target efficient near-infrared fluorescent probes: synthesis, in vitro evaluation, and in vivo imaging. Anal. Chem. 88, 1944–1950 (2016). [PubMed: 26717442]
33. Seo Y et al. A smart near-infrared fluorescence probe for selective detection of tau fibrils in Alzheimer's disease. ACS Chem. Neurosci. 7, 1474–1481 (2016). [PubMed: 27576176]
34. Park KS et al. A difluoroboron β-diketonate probe shows 'turn-on' near-infrared fluorescence specific for tau fibrils. ACS Chem. Neurosci. 8, 2124–2131 (2017). [PubMed: 28737890]
35. Ni R et al. Detection of cerebral tauopathy in P301L mice using high-resolution large-field multifocal illumination fluorescence microscopy. Biomed. Opt. Express 11, 4989–5002 (2020). [PubMed: 33014595]
36. Tagai K et al. High-contrast in vivo imaging of Tau pathologies in Alzheimer's and non-Alzheimer's disease tauopathies. Neuron 109, 42–58.e8 (2021). [PubMed: 33125873]

37. Park KS et al. A curcumin-based molecular probe for near-infrared fluorescence imaging of tau fibrils in Alzheimer's disease. Org. Biomol. Chem. 13, 11194–11199 (2015). [PubMed: 26488450]
38. Hyun H et al. Central C-C bonding increases optical and chemical stability of NIR fluorophores. RSC Adv. 4, 58762–58768 (2014). [PubMed: 25530846]
39. Yang C et al. ZW800-PEG: a renal clearable zwitterionic near-infrared fluorophore for potential clinical translation. Angew. Chem. Int. Ed. 60, 13847–13852 (2021).
40. Landsman MLJ, Kwant G, Mook GA & Zijlstra WG Light absorbing properties, stability, and spectral stabilization of indocyanine green. J. Appl. Physiol. 40, 575–583 (1976). [PubMed: 776922]
41. Choi HS et al. Synthesis and in vivo fate of zwitterionic near-infrared fluorophores. Angew. Chem. Int. Ed. 50, 6258–6263 (2011).
42. Raymond SB, Boas DA, Bacskai BJ & Kumar ATN Lifetime-based tomographic multiplexing. J. Biomed. Opt. 15, 046011 (2010). [PubMed: 20799813]
43. Venugopal V, Chen J, Lesage F & Intes X Full-field time-resolved fluorescence tomography of small animals. Opt. Lett. 35, 3189–3191 (2010). [PubMed: 20890329]
44. Jankowsky JL et al. Mutant presenilins specifically elevate the levels of the 42 residue β-amyloid peptide in vivo: evidence for augmentation of a 42-specific γ secretase. Hum. Mol. Genet. 13, 159–170 (2004). [PubMed: 14645205]
45. Santacruz K et al. Tau suppression in a neurodegenerative mouse model improves memory function. Science 309, 476–481 (2005). [PubMed: 16020737]
46. Rajamohamedsait HB & Sigurdsson EM Histological staining of amyloid and pre-amyloid peptides and proteins in mouse tissue. Methods Mol. Biol. 849, 411–424 (2012). [PubMed: 22528106]
47. Kwan AC, Duff K, Gouras GK & Webb WW Optical visualization of Alzheimer's pathology via multiphoton-excited intrinsic fluorescence and second harmonic generation. Opt. Express 17, 3679–3689 (2009). [PubMed: 19259208]
48. Shirani H et al. A palette of fluorescent thiophene-based ligands for the identification of protein aggregates. Chemistry 21, 15133–15137 (2015). [PubMed: 26388448]
49. Calvo-Rodriguez M et al. In vivo detection of tau fibrils and amyloid β aggregates with luminescent conjugated oligothiophenes and multiphoton microscopy. Acta Neuropathol. Commun. 7, 171 (2019). [PubMed: 31703739]
50. Banks WA Characteristics of compounds that cross the blood-brain barrier. BMC Neurology 9, S3 (2009). [PubMed: 19534732]
51. Minogue AM et al. Age-associated dysregulation of microglial activation is coupled with enhanced blood-brain barrier permeability and pathology in APP/PS1 mice. Neurobiol. Aging 35, 1442–1452 (2014). [PubMed: 24439957]
52. Ohtsuki S & Terasaki T Contribution of carrier-mediated transport systems to the blood-brain barrier as a supporting and protecting interface for the brain; importance for CNS drug discovery and development. Pharm. Res. 24, 1745–1758 (2007). [PubMed: 17619998]
53. Sanchez-Covarrubias L, Slosky L, Thompson B, Davis T & Ronaldson P Transporters at CNS barrier sites: obstacles or opportunities for drug delivery? Curr. Pharm. Des. 20, 1422–1449 (2014). [PubMed: 23789948]
54. Kuchibhotla KV et al. Aβ plaques lead to aberrant regulation of calcium homeostasis in vivo resulting in structural and functional disruption of neuronal networks. Neuron 59, 214–225 (2008). [PubMed: 18667150]
55. Wang T et al. Three-photon imaging of mouse brain structure and function through the intact skull. Nat. Methods 15, 789–792 (2018). [PubMed: 30202059]
56. Pologruto TA, Sabatini BL & Svoboda K ScanImage: flexible software for operating laser scanning microscopes. Biomed. Eng. Online 2, 13 (2003). [PubMed: 12801419]
57. Choi HS et al. Targeted zwitterionic near-infrared fluorophores for improved optical imaging. Nat. Biotechnol. 31, 148–153 (2013). [PubMed: 23292608]

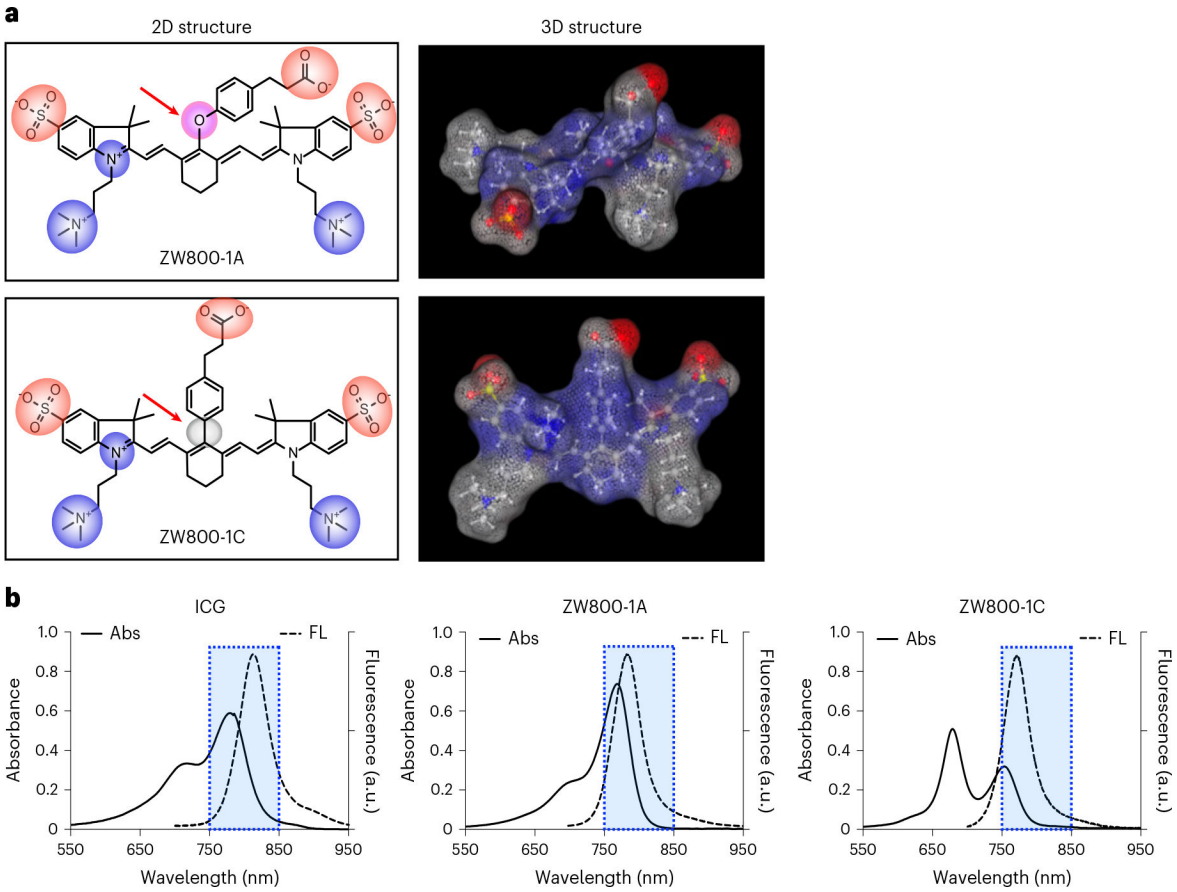

Fig. 1 |. Candidate heptamethine NIR fluorophores for AD imaging.

a, The chemical structures of ZW800–1A and ZW800–1C. The 3D energy-minimized structures were calculated by MarvinSketch (ChemAxon) to compare their hydrophobicity and conformational differences. **b**, The absorption and fluorescence spectra of candidate NIR fluorophores: ICG, ZW800–1A and ZW800–1C.

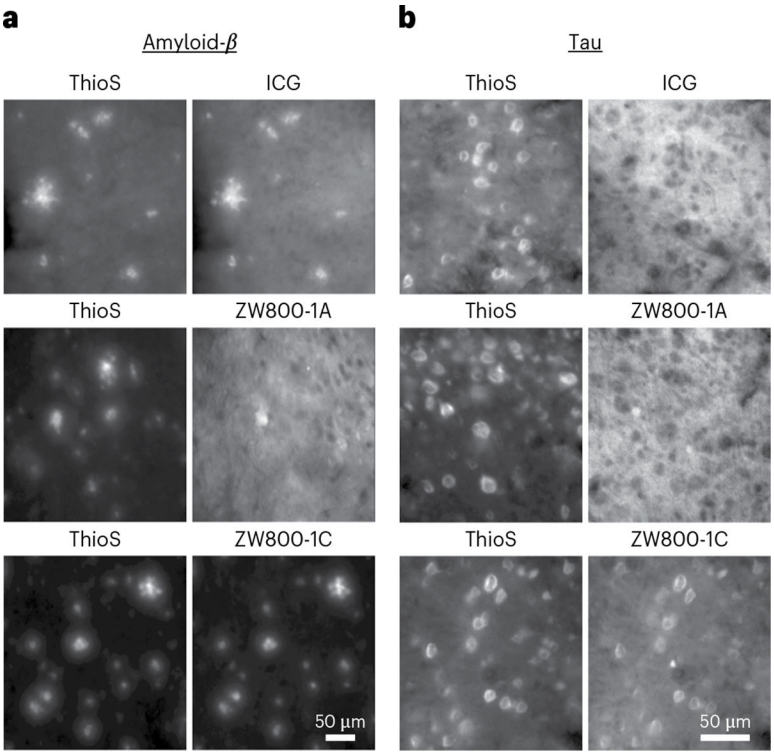

Fig. 2 |. Ex vivo imaging of amyloid plaques and NFTs in APP/PS1 and rTg4510 mouse brain sections.

a,**b**, APP/PS1 (**a**) and rTg4510 (**b**) mouse brain tissue sections co-stained with ThioS (0.05%) and each NIR fluorophore (100 μM). Images were acquired with widefield epifluorescence imaging in the green (for ThioS) and NIR channels.

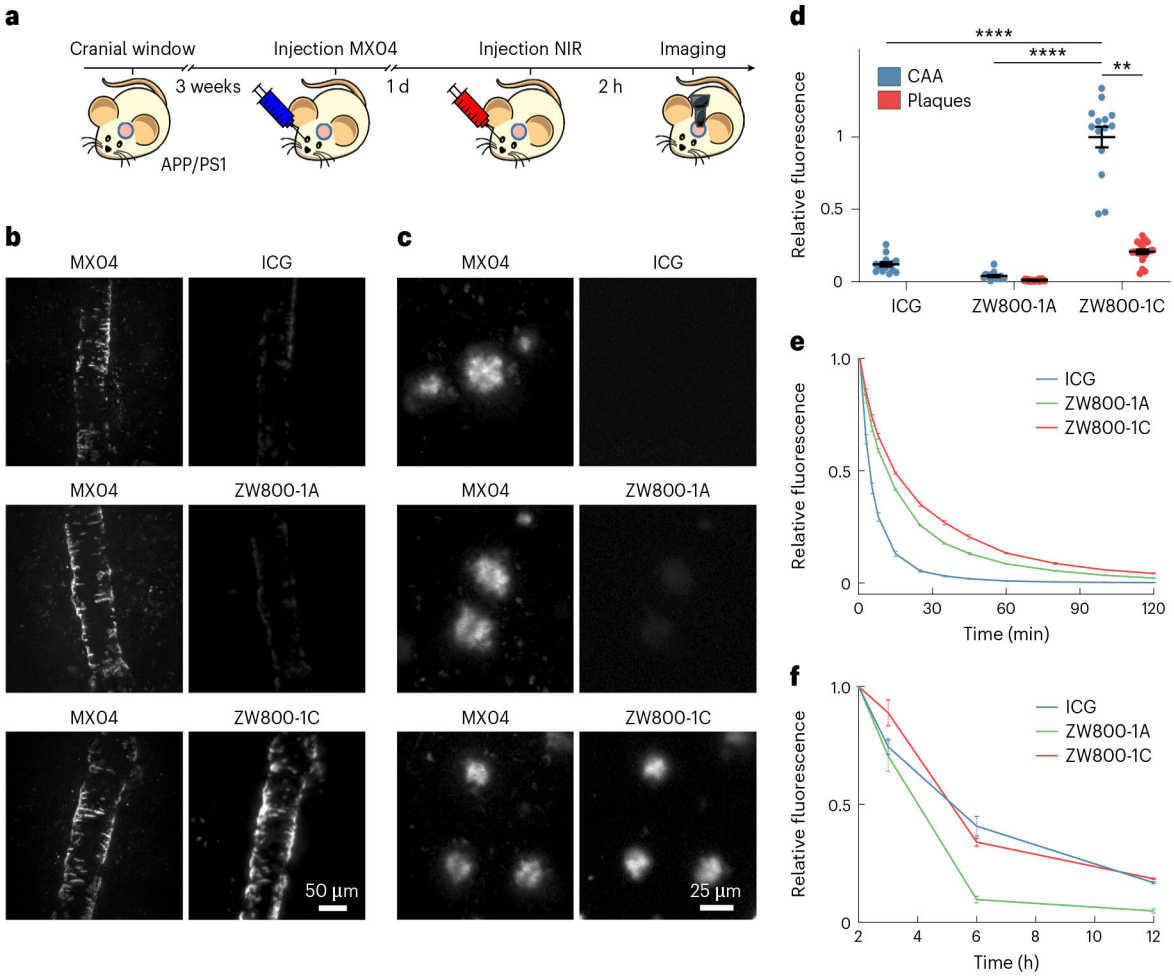

Fig. 3 |. In vivo imaging of amyloid plaques and CAA with ICG, ZW800–1A and ZW800–1C in APP/PS1 mice.

a, Experimental protocol for validation of binding to amyloid-β aggregates by candidate NIR fluorophores. MX04 was administered by intraperitoneal injection 1 d before imaging, and each NIR fluorophore was injected intravenously (50 nmol) 2 h before imaging with confocal microscopy. **b**,**c**, Representative images showing co-labelling of CAA (**b**) and plaques (**c**) by MX04 and each NIR fluorophore ($n = 3$ APP/PS1 Tg mice per fluorophore). Intensity was normalized relative to the brightest images (ZW800–1C for both CAA and plaques). **d**, Quantitative comparison of the average labelling intensity of CAA and plaques by each NIR fluorophore. For each NIR fluorophore, 6–8 volumes containing plaques and 4–5 volumes containing CAA were acquired per mouse from $n = 3$ APP/PS1 Tg mice. Significance was calculated using one-way ANOVA with Tukey's multiple comparisons test: ****$P < 0.0001$ and unpaired two-tailed t-test: **$P = 0.001$. **e**, The blood circulation dynamics of each NIR fluorophore from $n = 3$ C57BL/6J mice. **f**, Quantitative analysis of the fluorescence intensity of each NIR fluorophore bound to amyloid aggregate from $t = 2$ h to $t = 12$ h after injection. The intensities are normalized to $t = 2$ h from $n = 3$ APP/PS1 Tg mice per fluorophore. Data are shown as mean ± s.e.m.

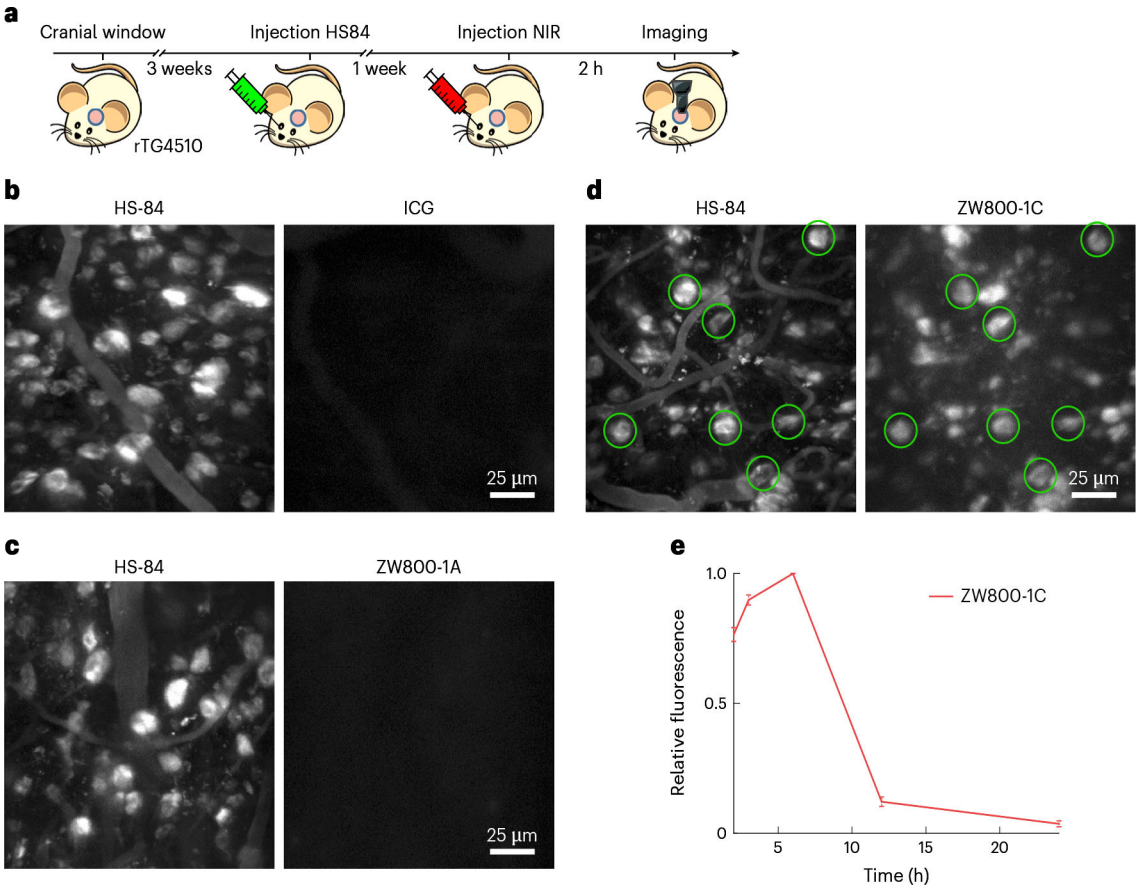

Fig. 4 |. In vivo imaging of NFTs with ICG, ZW800–1A and ZW800–1C in rTg4510 mice. **a**, Experimental protocol to validate labelling of NFTs by candidate NIR fluorophores. rTg4510 mice were intravenously injected with HS-84, a visible wavelength LCO, for labelling of NFTs 7 d before imaging. Mice were intravenously injected with each NIR fluorophore (50 nmol), and in vivo imaging by confocal microscopy was performed 2 h after injection. **b**–**d**, Representative images show co-labelling of NFTs by HS-84 and ICG (**b**), ZW800–1A (**c**) or ZW800–1C (**d**) ($n = 3$ rTg4510 Tg mice per fluorophore). The intensity of the NIR image was normalized to the brightest image (ZW800–1C). There was no apparent labelling of NFTs by either ICG or ZW800–1A. **e**, Quantitative analysis of the fluorescent intensity of ZW800–1C bound to NFTs from $t = 2$ h to $t = 24$ h after injection. The intensity was normalized to $t = 6$ h from $n = 2$ rTg4510 Tg mice. Data are shown as mean ± s.e.m.

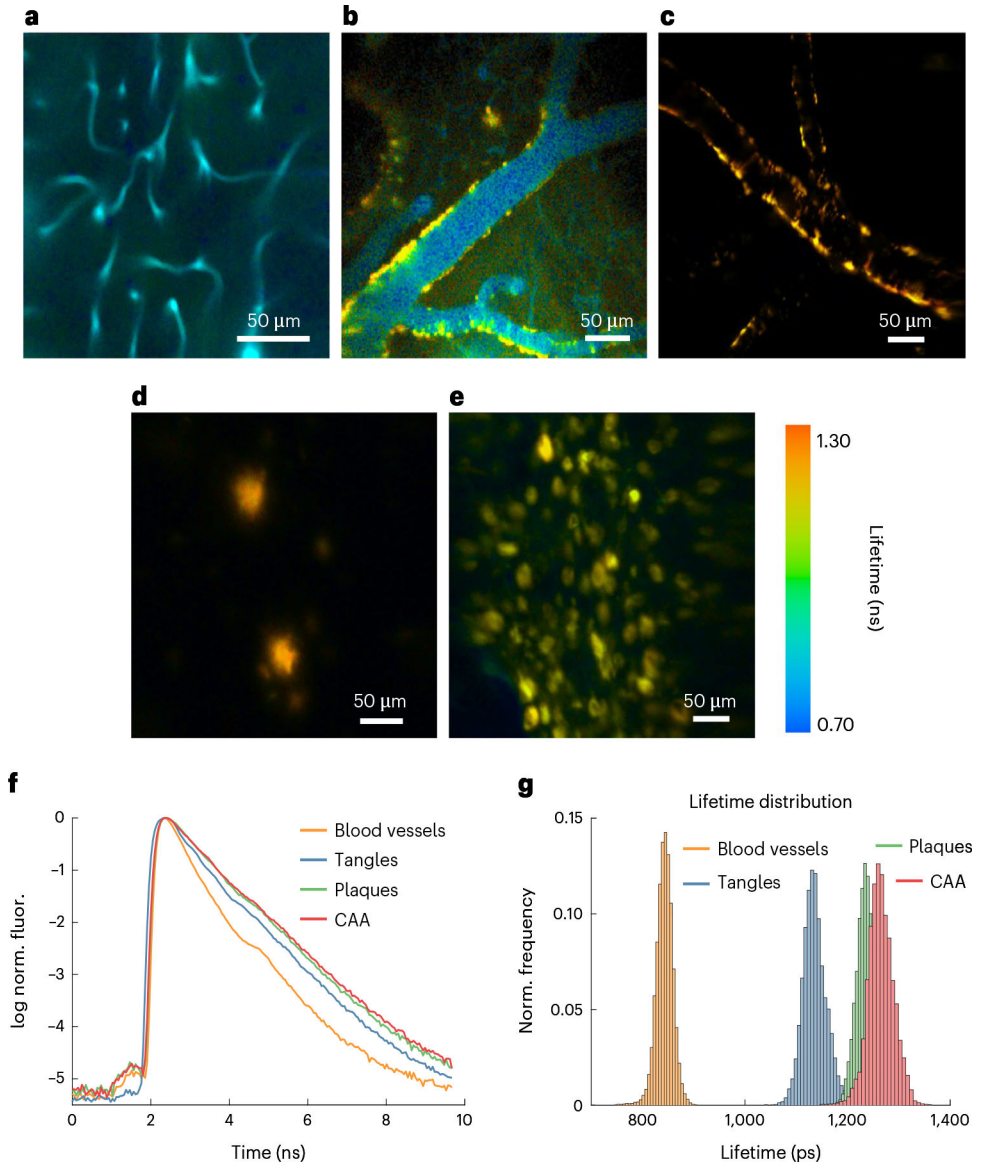

Fig. 5 |. In vivo fluorescence lifetime imaging of ZW800–1C in C57BL/6J, APP/PS1 and rTg4510 mice.

a–**e**, Representative FLIM images of ZW800–1C showing blood vessels (**a**), early-stage labelling of CAA 18 min post-injection (**b**), CAA (**c**), amyloid plaque (**d**) and NFT labelling 2 h post-injection (**e**). **f**, Average fluorescence temporal decay curves within blood vessels and after binding to amyloid-β and tau aggregates. **g**, Histogram distribution of fluorescence lifetimes within blood vessels and after being bound to amyloid-β and tau aggregates.

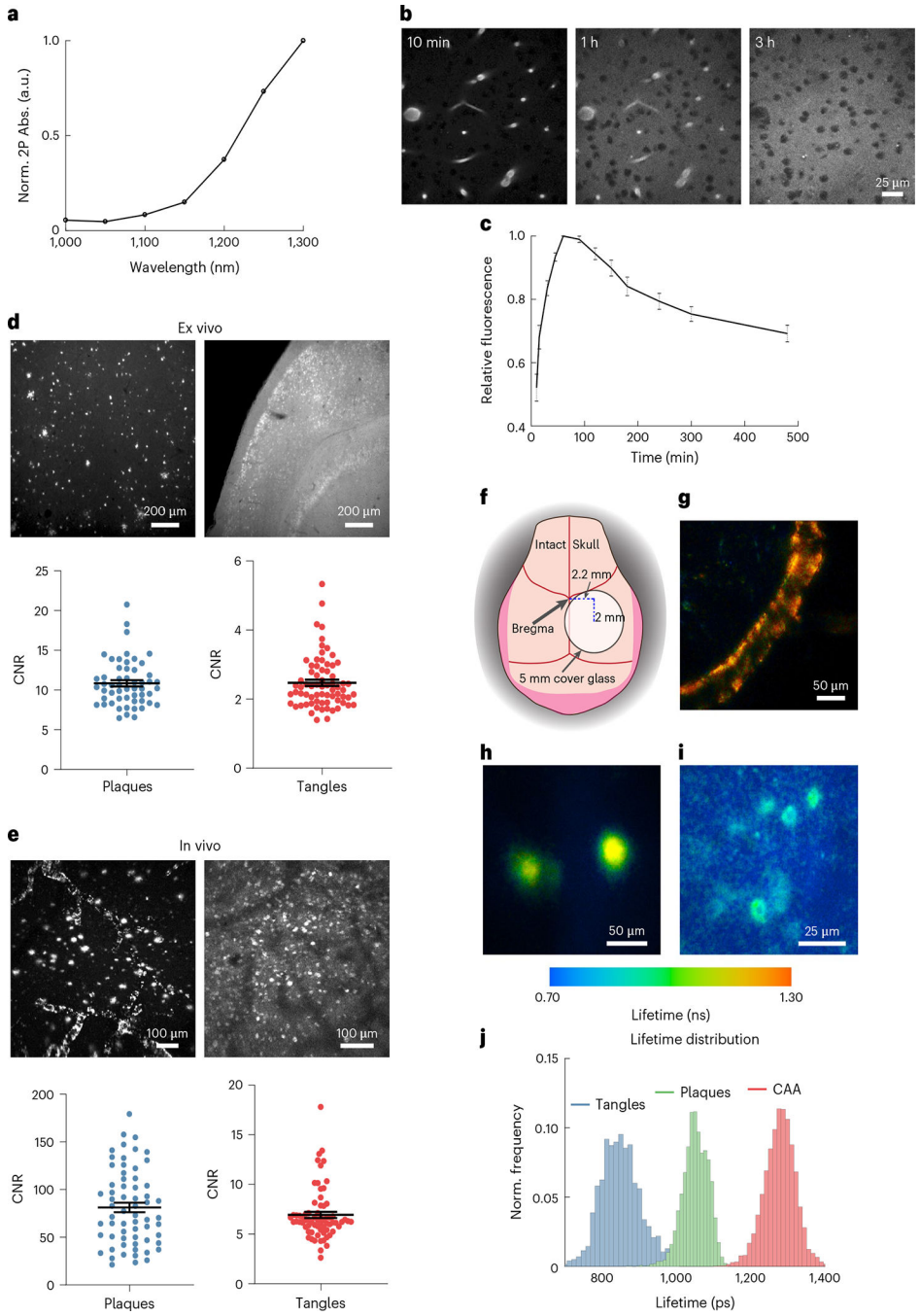

Fig. 6 |. Two-photon microscopy and non-invasive lifetime imaging of AD pathology with ZW800–1C.

a, Two-photon absorption spectrum of ZW800–1C. **b**, Time-lapse images of ZW800–1C fluorescence in brain parenchyma of C57BL/6J mice after intravenous injection. **c**, Clearance dynamics of ZW800–1C out of the brain from $t = 10$ min to $t = 8$ h from $n = 3$ C57BL/6J mice. **d**,**e**, Quantitative CNR analysis comparing ex vivo (**d**) and in vivo (**e**) detection of amyloid plaques and neurofibrillary tangles using two-photon microscopy. Top panels show representative images while bottom panels show CNR of individual

plaques and tangles. **f**, Schematic showing the region on the intact skull for non-invasive through-the-skull imaging. **g**–**i**, Representative images from $n = 3$ APP/PS1 Tg and $n = 3$ rTg4510 Tg mice demonstrating non-invasive lifetime imaging of CAA (**g**), amyloid plaques (**h**) and neurofibrillary tangles (**i**) through the intact skull using ZW800–1C (100 nmol). **j**, Histogram distribution of fluorescence lifetimes acquired through the intact skull after binding to AD pathology. Data are shown as mean ± s.e.m.

Table 1 |

Physicochemical properties of ZW800-1A and ZW800-1C

Fluorophore	**ZW800-1A**	**ZW800-1C**
Molecular weight (Da)	944.24	928.24
Charges (+/−)	+3/−3	+3/−3
Log*P*	−0.61	−0.24
Log*D*, pH 7.4	−3.35	−2.80
TPSA (Å^2)	167.18	157.95
HBA/HBD	10/1	8/1
Rotatable bonds	18	17

Log*P*, partition coefficient; log*D*, distribution coefficient; TPSA, topological polar surface area; HBA, hydrogen bond acceptors; HBD, hydrogen bond donors.